Electromagnetic Science
vol. 4, no. 2, 0140242, June 2026
https://doi.org/10.23919/emsci.2025.0024

Special Focus on Electromagnetic Information Theory

RESEARCH ARTICLE

Constitutive-Parameter-Driven Angular Metasurfaces

Qihao Lv[1], Yufei Zhao[1], Yong Liang Guan[1], Cheng Jin[2], Yue Li[3,4], and Chau Yuen[1]

1. *School of Electrical and Electronic Engineering, Nanyang Technological University, Singapore 639798, Singapore*
2. *School of Cyberspace Science and Technology, Beijing Institute of Technology, Beijing 100081, China*
3. *Department of Electronic Engineering, Tsinghua University, Beijing 100084, China*
4. *Beijing National Research Center for Information Science and Technology, Tsinghua University, Beijing 100084, China*

Corresponding authors: Yufei Zhao, Email: Yufei.zhao@ntu.edu.sg; Yong Liang Guan, Email: eylguan@ntu.edu.sg; Yue Li, Email: lyee@tsinghua.edu.cn.

Received May 2, 2025; Accepted September 12, 2025; Published Online September 26, 2025.

Abstract — Metasurfaces have revolutionized electromagnetic wave modulation across both the frequency and time domains, yet angular modulation remains underdeveloped due to the lack of analytical relationships between angular performance and structure, as well as unclear angular performance boundaries. To bridge these gaps, this work introduces a universal "angular response–constitutive parameter–metasurface structure" tripartite design paradigm, in which constitutive parameters serve as the core bridge directly mapping angular performance to metasurface structures. Analytical formulas are derived to establish the relationships between angular performance and constitutive parameters and to obtain the physical boundaries of angular performance. Subsequently, leveraging the known mapping between resonant structures and constitutive parameters in the Drude-Lorentz dispersion, folded resonators are employed to induce the required dispersive responses for pre-calculated constitutive parameters, thereby realizing a metasurface with an angular bandwidth of 19.2° and an angular selectivity of 1.51. Compared with conventional approaches, this paradigm eliminates the inherent trial-and-error process of structural selection, removing reliance on extensive and non-generalizable numerical simulations, while retaining only minor simulations for final optimizations. This work paves the way for advanced angular functionalities such as beam shaping and spatial-wave computation, promising potential applications in anti-interference communications, image edge detection, and multi-view holography.

Keywords — Angular modulation, Angular bandwidth, Angular selectivity, Constitutive parameters, Metasurfaces.

Citation — Qihao Lv, Yufei Zhao, Yong Liang Guan, *et al*., "Constitutive-parameter-driven angular metasurfaces," *Electromagnetic Science*, vol. 4, no. 2, article no. 0140242, 2026. doi: 10.23919/emsci.2025.0024.

I. Introduction

Electromagnetic (EM) metasurfaces have undergone transformative theoretical and technological advancements since their inception, revolutionizing wave modulation through subwavelength resonators [1], [2]. Early developments focused primarily on frequency-domain modulation using metallic resonators with frequency-related dimensions for amplitude, phase, and polarization control [3]. These advancements have led to remarkable applications in diverse fields such as wireless communications [4], radar radomes [5], imaging [6]–[8], metalenses [9]–[11], and quantum manipulation [12], [13]. Among these applications, fundamental modulation mechanisms have emerged via strategic resonator combinations: amplitude control by means of hybrid reflective/transmissive resonators [14]–[19], phase manipulation through phase-delay branches and geometric tuning [20], [21], and polarization control using rotational resonators and orthogonal metallic grids [22]–[24]. By integrating these resonators, the properties of EM waves can be effectively tailored.

More recently, metasurface capabilities have extended into the time domain through the integration of dynamically reconfigurable components, such as diodes [25]–[28], liquid crystals [29], [30], and graphene [31]. The incorporation of these reconfigurable components with control systems based on field-programmable gate array (FPGA) enables real-time wave modulation, unlocking new physical phenomena in time-domain functions such as dynamic beam steering, multi-harmonic control, and adaptive scattering [32]. These developments have catalyzed novel applications in active camouflage [33], anti-interference com-

Electromagnetic Science

munications [34], holography [35], and multi-target communication [36].

With the growing demand for spatial modulation of EM waves, metasurfaces capable of tailoring EM waves in the angular domain, namely angular metasurfaces, have attracted considerable attention. However, research in this area is still in its early stages. Initial studies were motivated by structural miniaturization aimed at enhancing angular stability [37], but the quantitative relationship between the degree of miniaturization and the angular response remains elusive. Meanwhile, ultra-wide-angle transmissive metasurfaces based on the generalized Brewster phenomenon have been developed to ensure stable performance in non-cooperative scenarios [38], [39]. In addition, metasurfaces utilizing multi-order grating modes [40] or high-order electric/magnetic multipolar resonance interference [41] have been proposed to achieve wide-angle and even omnidirectional reflection. Beyond the Brewster-inspired approaches, photonic-crystal-based transparent media with shifted equal-frequency contours (EFCs) have been proposed to achieve omnidirectional impedance matching [42], and dielectric metamaterials capable of restoring effective self-duality have been demonstrated to realize polarization independence and omnidirectional impedance matching [43]. Moreover, by separating the EFCs of different materials, ultra-compact photonic circuits without cladding layers have been achieved, offering both omnidirectional transmission and negligible inter-channel crosstalk [44].

Subsequently, the concept of angle-selective surfaces was proposed, and the qualitative effects of various resonator types on angular performance were investigated using equivalent conductance models [45]–[47]. Then, by stacking multilayer photonic crystals to overlap the angular photonic bandgaps, polarization-independent broadband angle-selective properties were achieved [48], while magnetic metamirrors functioning as spatial-frequency filters were realized based on the coupled-mode theory and equivalent transmission-line models [49]. However, due to the absence of analytical relationships between angular responses and physical structures, current angular metasurface designs still critically rely on computationally extensive numerical optimization, particularly for multilayer metasurface design, an approach that is both time-consuming and may not guarantee optimal solutions. Additionally, the theoretical understanding of angular performance boundaries remains unclear. Consequently, it is imperative to establish a precise analytical framework for angular metasurfaces, along with corresponding design methodologies comparable to those developed for frequency- and time-domain metasurfaces.

To bridge these critical gaps, this work proposes a universal "angular response–constitutive parameter–metasurface structure" tripartite design paradigm for angular metasurfaces. Herein, analytical relationships between constitutive parameters and the angular response of metasurfaces are theoretically derived, along with the angular response boundaries for single-layer metasurfaces. Subsequently, based on the known analytical mapping between electrical/magnetic resonances and metasurface constitutive parameters in the Drude-Lorentz dispersion, a practical metasurface is realized by employing folded resonators to produce the desired dispersive response. In this paradigm, constitutive parameters serve as the core bridge that directly links the angular response and structure of metasurfaces. In stark contrast to conventional approaches, this paradigm eliminates the inherent trial-and-error process in structural selection, fundamentally removing reliance on extensive numerical simulations while retaining only minor simulations for final structural optimization. This work pioneers a precise and universal design paradigm for angular metasurface engineering, promising potential applications in anti-interference communications, image edge-detection, and multi-view holography.

II. Theoretical Analysis

Given the finite nature of the angular domain, mechanically rotating a lowpass transmissive angular metasurface enables functionalities analogous to those in the frequency and time domains, namely lowpass, bandpass, and highpass transmission, as shown in Figure 1(a). Therefore, this study focuses on metasurfaces with lowpass angular transmission characteristics, whose responses are characterized by two key parameters: angular bandwidth (ABW) and angular selectivity (AS), as shown in Figures 1(b) and 1(c). Specifically, angular bandwidth is defined as the angular range over which the transmission coefficient exceeds −3 dB, while angular selectivity is defined as the ratio of the angular ranges where the transmission coefficient exceeds −10 dB and −3 dB, respectively. For clarity, the angles at which the transmission coefficients reach −10 dB and −3 dB are referred to as rejection angle θ_s and cutoff

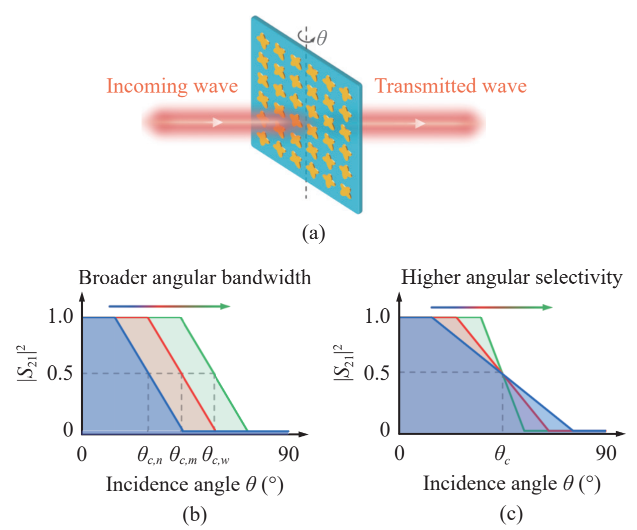

Figure 1 Schematic illustrations of (a) A transmissive metasurface under oblique incidence and its angular response with different (b) Angular bandwidths and (c) Angular selectivity, where θ_c represents the cutoff angle, and the subscripts n, m, and w donotes the narrow band, middle band, and wide band, respectively.

angle θ_c, respectively ($|S_{21}(\theta_s)| = -10$ dB and $|S_{21}(\theta_c)| = -3$ dB). Accordingly, the angular bandwidth and angular selectivity are calculated as $\text{ABW} = \theta_c$ and $\text{AS} = \theta_s / \theta_c$, respectively. Unless otherwise specified, all subsequent metasurface parameters are described in the angular domain rather than in the traditional frequency domain.

1. Angular response of metasurfaces

The transmission (S_{21}) and reflection (S_{11}) coefficients of a metasurface under oblique incidence are governed by its constitutive parameters, namely the relative permittivity and permeability. Notably, the angular responses of metasurfaces for transverse electric (TE) and transverse magnetic (TM) polarizations exhibit a form of duality: Identical angular behavior is observed when the relative permittivity and permeability are interchanged. Therefore, for simplicity and without loss of generality, only the TE-polarized case is analyzed in the following, while that of the TM-polarized case can be obtained by interchanging the relative permittivity and permeability [38].

Herein, a uniaxial anisotropic metasurface with subwavelength thickness is considered, in which the relative permittivity and permeability are both in diagonal tensor form:

$$\bar{\bar{\boldsymbol{\varepsilon}}}_m = \begin{bmatrix} \varepsilon_t & 0 & 0 \\ 0 & \varepsilon_t & 0 \\ 0 & 0 & \varepsilon_n \end{bmatrix}, \quad \bar{\bar{\boldsymbol{\mu}}}_m = \begin{bmatrix} \mu_t & 0 & 0 \\ 0 & \mu_t & 0 \\ 0 & 0 & \mu_n \end{bmatrix} \tag{1}$$

where the subscripts t and n denote the tangential and normal components of the relative permittivity and permeability, respectively. In this regard, the transmission and reflection coefficients of the metasurface can be written as [50]

$$S_{21} = \frac{(1-r^2)\mathrm{e}^{-\mathrm{j}\varphi}}{1-r^2\mathrm{e}^{-\mathrm{j}2\varphi}}, \quad S_{11} = \frac{r(1-\mathrm{e}^{-\mathrm{j}2\varphi})}{1-r^2\mathrm{e}^{-\mathrm{j}2\varphi}} \tag{2}$$

where r is the reflection coefficient at the air–metasurface interface, and φ is the phase change within the metasurface. The interface reflection r is given by [38]

$$r = \frac{\cos\theta - \sqrt{\dfrac{\varepsilon_t}{\mu_t} - \dfrac{\sin^2\theta}{\mu_t\mu_n}}}{\cos\theta + \sqrt{\dfrac{\varepsilon_t}{\mu_t} - \dfrac{\sin^2\theta}{\mu_t\mu_n}}} \tag{3}$$

and the corresponding phase change φ is given by

$$\varphi = k_0 h \mu_t \sqrt{\frac{\varepsilon_t}{\mu_t} - \frac{\sin^2\theta}{\mu_t\mu_n}} \tag{4}$$

where $k_0 = 2\pi/\lambda_0$ is the free-space wavenumber, λ_0 is the operating wavelength, and h is the metasurface thickness. For a subwavelength metasurface, where $h \ll \lambda_0$, the phase change φ typically remains below π. This is due to the limited magnetic density in practical metasurfaces [51].

2. Constitutive parameter conditions

For lowpass angular metasurfaces, the transmission coefficient is ideally unity at normal incidence, i.e., $|S_{21}|_{\theta=0} = 1$, and gradually decreases as the incidence angle increases. In this case, based on (2), the following two conditions are obtained:

$$r|_{\theta=0} = 0 \ \text{ and } \ \varphi|_{\theta\in(0,90^\circ)} \neq n\pi, \quad n \in \mathbb{N} \tag{5a}$$

$$r|_{\theta\in(0,90^\circ)} \neq 0 \ \text{ and } \ \varphi|_{\theta=0} = n\pi, \quad n \in \mathbb{N} \tag{5b}$$

From (5a), the condition for the metasurface constitutive parameters is as follows:

$$\varepsilon_t = \mu_t \tag{6}$$

For (5b), since the phase change φ is less than π, parameter n is set to zero, which corresponds to metasurfaces with zero constitutive parameters, including epsilon-near-zero (ENZ), mu-near-zero (MNZ), and epsilon-mu-near-zero (EMNZ) metasurfaces. As derived in Appendix A, only EMNZ metasurfaces can satisfy the initial assumption $|S_{21}|_{\theta=0} = 1$, whereas ENZ and MNZ metasurfaces fail to meet this criterion. Thus, the constitutive parameter condition for (5b) is as follows:

$$\varepsilon_t = \mu_t = 0 \tag{7}$$

which can be regarded as a special case of (6). Under these conditions, the interface reflection and phase change for the metasurface can be expressed as follows:

$$r_L = \frac{\cos\theta - \sqrt{1 - \dfrac{\sin^2\theta}{\mu_t\mu_n}}}{\cos\theta + \sqrt{1 - \dfrac{\sin^2\theta}{\mu_t\mu_n}}} \tag{8a}$$

$$\varphi_L = k_0 h \mu_t \sqrt{1 - \frac{\sin^2\theta}{\mu_t\mu_n}} \tag{8b}$$

Based on (2) and (8), the angular responses of metasurfaces are determined by three key parameters: the incidence angle θ, the phase factor $k_0 h \mu_t$, and the permeability factor $\mu_t\mu_n$. In the following, their angular responses, characterized by angular bandwidth and selectivity, are analyzed and derived with respect to their constitutive parameters.

3. Angular bandwidth of metasurface

The angular bandwidth of the lowpass transmissive metasurface, quantified by the cutoff angle θ_c, where $|S_{21}| = -3$ dB, is analyzed based on (2) and (8). Figure 2 illustrates the angular response of the metasurface, with the blue dashed lines representing the contours of the cutoff angle θ_c. Notably, the behavior of the cutoff angle differs significantly between regions $\mu_t\mu_n < 1$ and $\mu_t\mu_n > 1$. Specifically, when $\mu_t\mu_n < 1$, the cutoff angle varies from nearly 0 to nearly 90°.

Electromagnetic Science

This indicates that the angular bandwidth can be tuned from nearly zero to cover almost the entire angular domain. In contrast, for $\mu_t\mu_n > 1$, the cutoff angle spans only a limited portion of the large-angle domain, and its coverage mainly depends on the phase factor $k_0h\mu_t$. The following analysis discusses the analytical relationships between the cutoff angle, the phase factor, and the permeability factor for these two regions.

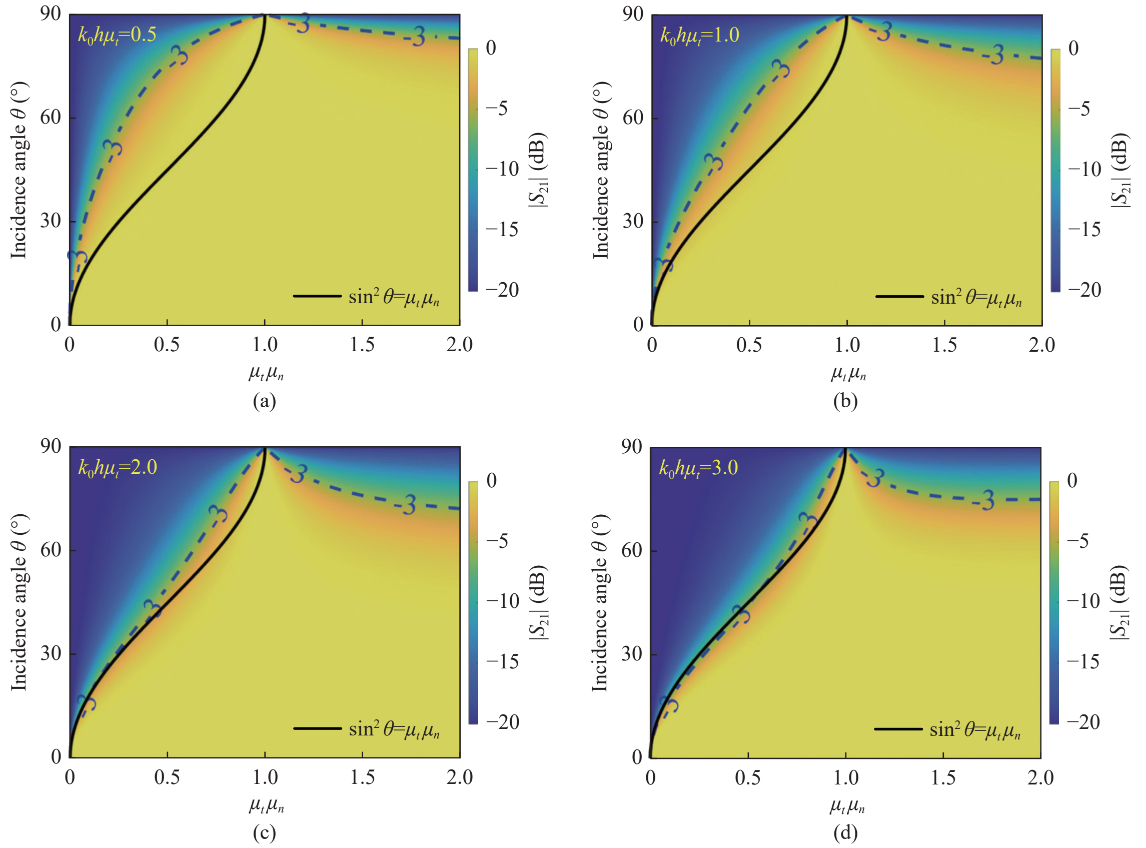

Figure 2 Angular response of a lowpass metasurface with the variation of incidence angle θ and parameter $\mu_t\mu_n$ under different values of $k_0h\mu_t$: (a) $k_0h\mu_t = 0.5$; (b) $k_0h\mu_t = 1.0$; (c) $k_0h\mu_t = 2.0$; (d) $k_0h\mu_t = 3.0$.

In the region where $\mu_t\mu_n < 1$, the θ_c increases monotonically with an increasing permeability factor $\mu_t\mu_n$ and a decreasing phase factor $k_0h\mu_t$. According to (2) and (8), the analytical relationship among these three parameters is governed by the real/imaginary nature of the root term $\sqrt{1-\sin^2\theta/\mu_t\mu_n}$. In Figure 2, the black solid curve denotes the real-imaginary boundary of this term. The upper region corresponds to imaginary values, whereas the lower region corresponds to real values. For a small phase factor, the cutoff angle contours lie entirely within the upper (imaginary) region. As the phase factor increases, these contours gradually intersect the real-imaginary boundary. The critical phase factor is derived to be 2, corresponding to the critical state where the cutoff angle curve first intersects the real-imaginary dividing line (detailed in Appendix B).

The relationship between the cutoff angle, the phase factor, and the permeability factor can be obtained from $|S_{21}| = |S_{11}|$. By combining (2), this expression can be further simplified to

$$\left|r_L^{-1} - r_L\right| = \left|\mathrm{e}^{\mathrm{j}\varphi_L} - \mathrm{e}^{-\mathrm{j}\varphi_L}\right| \tag{9}$$

Based on (9), their relationship exhibits different forms for different values of the phase factor ($k_0h\mu_t \le 2$ or $k_0h\mu_t > 2$). When the phase factor $k_0h\mu_t$ is less than or equal to 2, their relationship is derived as follows:

$$k_0h\mu_t = \frac{1}{A_N}\ln\frac{1+\sqrt{1+F_N^2}}{F_N} \tag{10}$$

in which $A_N = \sqrt{\sin^2\theta_c/\mu_t\mu_n - 1}$ and $F_N = (\cos^2\theta_c + A_N^2)/(2A_N\cos\theta_c)$ (detailed in Appendix C.1). When the phase factor $k_0h\mu_t$ exceeds 2, the cutoff angle spans both regions for different permeability factors, and the relationship is defined piecewise as follows:

$$\begin{cases} k_0h\mu_t = \dfrac{1}{A_P}\sin^{-1}(F_P), & 0 < \mu_t\mu_n \le 1 - \dfrac{4}{(k_0h\mu_t)^2} \\ k_0h\mu_t = \dfrac{1}{A_N}\ln\dfrac{1+\sqrt{1+F_N^2}}{F_N}, & 1 - \dfrac{4}{(k_0h\mu_t)^2} < \mu_t\mu_n \le 1 \end{cases} \tag{11}$$

where $A_P = \sqrt{1-\sin^2\theta_c/\mu_t\mu_n}$ and $F_P = 2A_P\cos\theta_c/(\cos^2\theta_c - A_P^2)$ (detailed in Appendix C.2). Figure 3 shows the relationship between the cutoff angle and the permeability factor for different phase factors based on (10) and (11). It is observed that the cutoff angle is positively correlated with the permeability factor and negatively correlated with the phase factor. Overall, the angular bandwidth of the metasurface can span a wide range from very narrow to nearly the entire angular domain, which can be flexibly tailored by adjusting the cutoff angle through modifications to thickness and constitutive parameters based on (10) and (11).

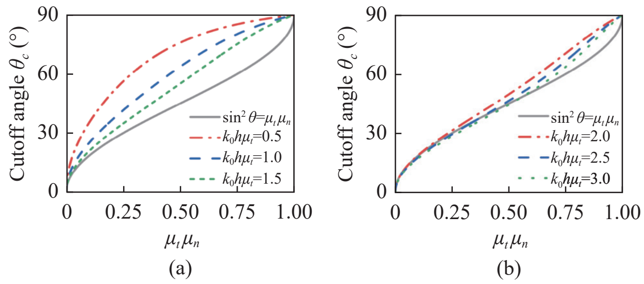

Figure 3 Angular response of the metasurface in the region of $\mu_t\mu_n < 1$ under cases of (a) $k_0h\mu_t < 2$ and (b) $k_0h\mu_t > 2$.

In the region where $\mu_t\mu_n > 1$, as shown in Figure 2, the cutoff angle appears only within the real region of the term $\sqrt{1-\sin^2\theta/\mu_t\mu_n}$ and continuously decreases from 90° as the permeability factor increases for different phase factors. Figure 4(a) displays the range of the cutoff angle with varying permeability factors and phase factors. The achievable cutoff angle range decreases as the phase factor increases, and the minimum cutoff angle occurs when the permeability factor $\mu_t\mu_n$ tends to infinity, in which case the cutoff angle can be expressed as follows:

$$\theta_c = \cos^{-1}\frac{\sqrt{\sin^2 k_0h\mu_t+1}-1}{\sin k_0h\mu_t}, \quad k_0h\mu_t \in [0,\pi] \tag{12}$$

According to (12), the minimum cutoff angle can be calculated as approximately 65.53° occurring when the permeability factor is infinite and the phase factor $k_0h\mu_t$ equals $\pi/2$, as depicted in Figure 4(b). Therefore, in the region $\mu_t\mu_n > 1$, the range of cutoff angle can only cover a partial large-angle domain of 65.53°–90.00°, resulting in metasurfaces in this region being limited and not considered in practical applications, and thus, in the following analysis, only the region $\mu_t\mu_n < 1$ is considered.

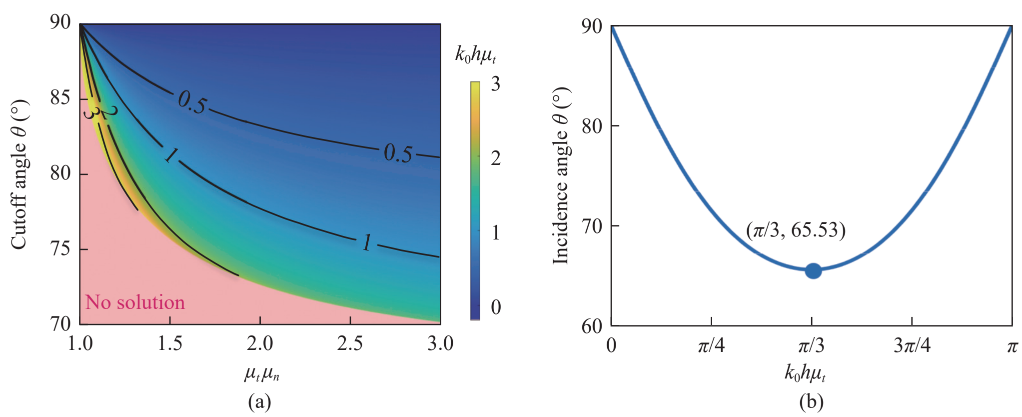

Figure 4 Range of cutoff angle θ_c for metasurfaces with variation of different phase factor $k_0h\mu_t$ in the region of $\mu_t\mu_n > 1$ under (a) Different permeability factors and (b) Infinite permeability factors.

Additionally, for the special case of a lowpass transmissive metasurface, i.e., the EMNZ metasurface, the cutoff angle θ_c which is derived from (A-17) in Appendix A is given as

$$\theta_c = \sin^{-1}\frac{\sqrt{(k_0h/\mu_n)^2+1}-1}{k_0h/\mu_n} \tag{13}$$

It is seen that the cutoff angle of EMNZ metasurfaces can be tailored from 0° to nearly 90° by enhancing the ratio of the phase factor to the permeability factor, i.e., k_0h/μ_n.

4. Angular selectivity of metasurface

The angular selectivity, defined by the ratio of the rejection angle to the cutoff angle (θ_s/θ_c), is another critical metric for evaluating angular response. Notably, the achievable range of angular selectivity for a given cutoff angle is inherently constrained, as the range of the rejection angle is limited. This range can be obtained by substituting all feasible combinations of the phase factor and the permeability factor, which are derived from (10) and (11) for a given cutoff angle, into (2).

Figure 5(a) illustrates the relationship between the phase factor and the permeability factor for varying cutoff angles. For a fixed cutoff angle, the phase factor and the permeability factor increase nonlinearly and synchronously from near-zero values. It is worth noting that the phase factor is limited to π to align with the previous assumption regarding subwavelength metasurface thickness ($k_0h\mu_t < \pi$). These combinations are then substituted into (2) and (8) to compute the corresponding ranges of the rejection angle and angular selectivity. As shown in Figure 5(b), the rejection angle exhibits a finite range, corresponding to the combinations of the phase factor and the permeability factor with minimum and maximum values, respectively. Figure 5(c) illustrates the resulting upper and lower boundaries of angular selectivity for each cutoff angle. Table 1 provides the ranges of the rejection angle and the corresponding angular selectivity for representative cutoff angles. For EMNZ metasurfaces, a special case of lowpass angular metasurfaces, the analytical relationship between the rejection angle θ_s and the cutoff angle θ_c can be derived from (A-17) in Appendix A as follows:

$$\theta_s = \cos^{-1}\left(\sqrt{1+\left(\frac{3\sin^2\theta_c}{2\cos\theta_c}\right)^2} - \frac{3\sin^2\theta_c}{2\cos\theta_c}\right) \tag{14}$$

which is visually presented in Figure 5(b) as the black solid line and lies along the upper boundary of the θ_s–θ_c region of lowpass angular metasurfaces. This relationship yields the highest values of angular selectivity, as displayed in Figure 5(c), and imposes a strict one-to-one correspondence between the two angles. Such strict dependence of angular selectivity on angular bandwidth limits the design flexibility in achieving various angular performances using EMNZ metasurfaces.

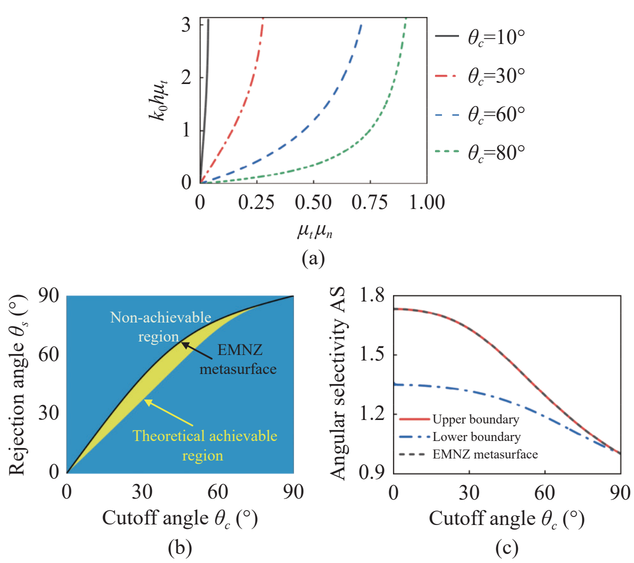

Figure 5 Relationship between the angular bandwidth and angular selectivity: (a) Relationship between the permeability factor $\mu_t\mu_n$ and the phase factor $k_0h\mu_t$ under different cutoff angles; Ranges of (b) Rejection angle θ_s and (c) Angular selectivity AS for lowpass angular metasurfaces, including EMNZ metasurfaces, with respect to the cutoff angle θ_c.

Table 1 Range of rejection angle and angular selectivity

Cutoff angle	Rejection angle range	Angular selectivity range
10°	13.47°–17.23°	1.35–1.72
20°	26.73°–33.84°	1.34–1.69
30°	39.52°–48.95°	1.32–1.63
40°	51.50°–61.50°	1.29–1.54
50°	62.21°–70.96°	1.24–1.42
60°	73.23°–77.75°	1.19–1.30
70°	81.35°–82.70°	1.12–1.18
80°	86.43°–86.59°	1.06–1.08

According to the above analysis, it is evident that a single-layer metasurface can achieve an angular bandwidth ranging from nearly 0° to nearly 90° while the angular selectivity remains inherently limited. Moreover, as the angular bandwidth increases, the achievable range of angular selectivity decreases. This trend indicates a trade-off between angular bandwidth and selectivity, which should be taken into account when designing angular metasurfaces for various applications.

Within the achievable angular response, the constitutive parameters of metasurfaces required for a specific response can be determined through the following steps:

i) Use ABW = θ_c and AS = θ_s/θ_c to calculate the cutoff angle θ_c and rejection angle θ_s for achieving the desired ABW and AS.

ii) Substitute the cutoff angle θ_c into (10) and (11) to obtain all feasible combinations of phase factor $k_0h\mu_t$ and permeability factor $\mu_t\mu_n$.

iii) Substitute each of these combinations from step ii) into (2) and (8) to calculate the corresponding rejection angle θ_s.

iv) Identify the appropriate combination of the phase factor $k_0h\mu_t$ and the permeability factor $\mu_t\mu_n$ that can achieve the desired rejection angle θ_s from the combinations in step iii), thereby obtaining the required constitutive parameters for the predefined angular response.

III. Simulation and Experimental Validation

1. Design of angular metasurface

Based on the known mapping between electrical/magnetic resonances and metasurface constitutive parameters within the Drude-Lorentz dispersion, a classical resonator is utilized to induce the desired dispersive behavior for the physical realization of a metasurface with a predefined angular response. Here, a representative case is presented. In this case, it has an angular bandwidth of 20° and an angular selectivity of 1.5, corresponding to cutoff and rejection angles of 20° and 30°, respectively, at an operating frequency of 10 GHz. The required constitutive parameters are derived as $\varepsilon_t = \mu_t$, $\mu_t\mu_n = 0.057$, and $k_0h\mu_t = 0.852$. To simplify the metasurface design, the tangential relative permeability μ_t is set to 1. Consequently, the required conditions for the metasurface constitutive parameters are further calculated as follows:

$$\varepsilon_t = \mu_t = 1,\ \mu_n = 0.057,\ \text{and}\ h = 0.4\ \text{mm} \tag{15}$$

Considering that the dielectric substrates used in metasurfaces have unity relative permeability, condition (15) can be satisfied by tailoring the tangential relative permittivity ε_t and the normal relative permeability μ_n. In this regard, loop-type resonators capable of constructing both linear and loop current paths are an optimal choice for inducing the electrical- and magnetic-type Drude-Lorentz dispersion to tune ε_t and μ_n at the desired frequency [52].

As displayed in Figures 6(a) and 6(b), the metasurface unit cell is composed of a folded square metallic loop printed on a 0.4 mm-thick dielectric substrate with a relative permittivity $\varepsilon_r = 3$ and a loss tangent $\tan\delta = 0.013$. The unit cells are periodically arranged along the x- and y-axes with a period $P = 10$ mm. The sidelength and linewidth of the square loop are $L_s = 9.8$ mm and $W_s = 0.3$ mm, respectively, while the folded components are characterized by an embedded length $L_{\text{in}} = 3.2$ mm, an embedded width $W_{\text{in}} = 0.9$ mm, and an offset distance $D = 3.6$ mm, respectively. Figure 6(c) displays the angular response of the optimized metasurface, which is consistent with the results calculated from (2), (8), and (15). It is observed that the designed metasurface achieves cutoff and rejection angles of 19.8° and 30.4°, respectively, at 10 GHz, yielding an angular bandwidth of 19.8° and an angular selectivity of 1.53, both of which closely match the predefined objectives. In addition, since the theoretical analysis does not account for substrate loss, the angular responses of the designed metasurface with and without substrate loss are further compared in Figure 6(c). The results demonstrate that the impact of substrate loss on angular performance is negligible.

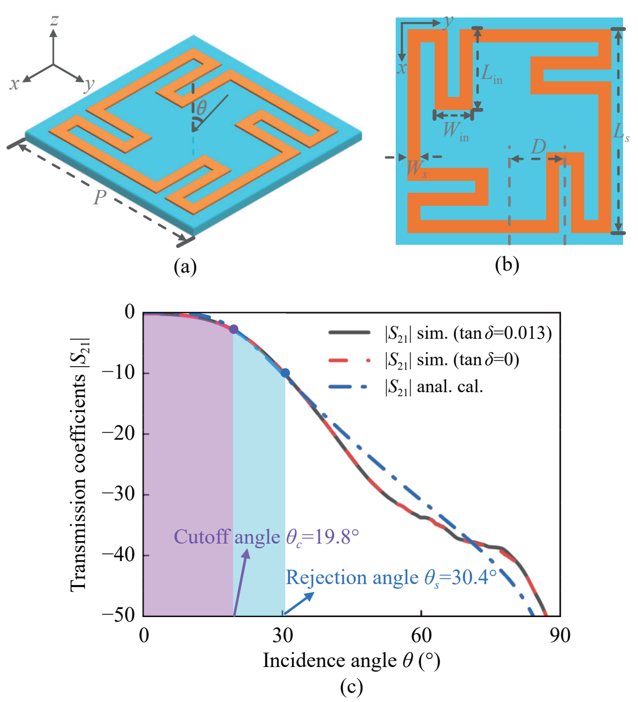

Figure 6 Structure and performance: (a) Perspective and (b) Top view of the designed angular metasurface; (c) Simulated angular response of the designed angular metasurface with and without substrate loss together with analytically calculated one.

2. Analysis of the designed angular metasurface

In the angular metasurface illustrated in Figure 6(a), periodic loop-type resonators are employed to tune the constitutive parameters ε_t and μ_n. Specifically, an electrical-type Drude–Lorentz dispersion is stimulated through constructing linear current paths aligned with the direction of the tangential electric field of incident EM waves, as depicted in Figure 7(a), thereby enabling the tailoring of the constitutive parameter ε_t. By varying the total circumference of the resonators, their electrical resonance characteristics are modulated to tailor the structural permittivity. To meet the desired condition for ε_t, the metasurface is designed to operate in the high-frequency non-resonant region. Meanwhile, as shown in Figure 8, the employed loop-type resonators are folded to miniaturize the metasurface periodicity, thereby suppressing the influence of grating lobes in the high-frequency region on the constitutive parameters. In this manner, as illustrated in Figure 8(a), the circumference of the resonator is controlled by adjusting the embedded length L_{in} of the folded components. Figure 8(b) reveals that the resonant frequency of the electrical-type Drude-Lorentz dispersion decreases from 3.56 GHz to 3.14 GHz as the embedded length increases from 1.6 mm to 3.2 mm. Correspondingly, the tangential relative permittivity ε_t at the operating frequency of 10 GHz increases from approximately −9.30 to 0.99, approaching the required condition.

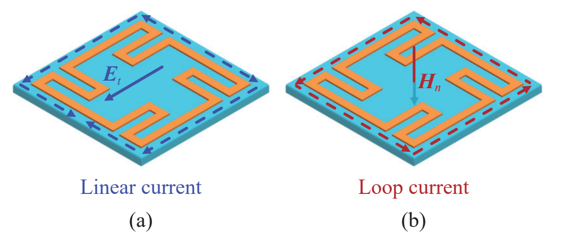

Figure 7 Current flow on the loop-type resonators stimulated by (a) Tangential electric field $\boldsymbol{E}_t$ and (b) Normal magnetic field $\boldsymbol{H}_n$ under oblique incidence.

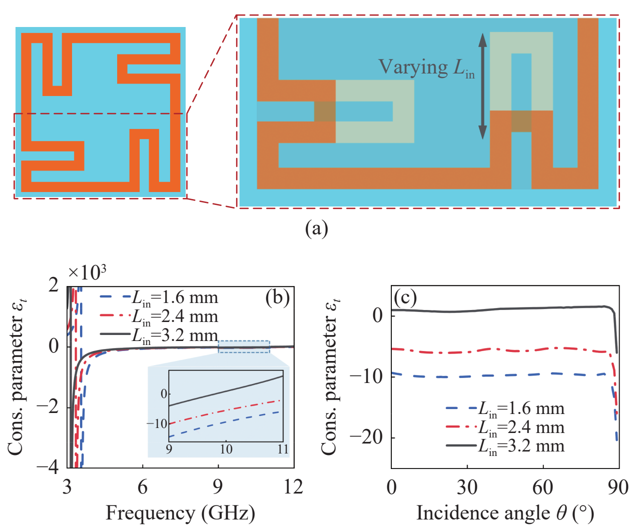

Figure 8 Influence of embedded length L_{in} on the constitutive parameter ε_t: (a) Schematic diagram of the variation in embedded length; (b) Frequency response and (c) Angular response at 10 GHz of the parameter ε_t with variation of L_{in}.

When the metasurface is illuminated by EM waves at an oblique incidence angle, the normal components of the magnetic field induce a magnetic-type Drude-Lorentz dispersion by constructing currents circulating around the resonators, as illustrated in Figure 7(b), thereby tailoring the constitutive parameter μ_n [53]. As displayed in Figure 9(a), the resonant characteristics of this magnetic response can be tailored by adjusting the offset distance of the folded components. Figure 9(c) demonstrates that the resonant frequency of the magnetic resonance shifts from 5.66 GHz to 8.22 GHz as the offset distance D increases from 0 mm to 3.6 mm. Correspondingly, the normal relative permeability μ_n at 10 GHz decreases from 0.133 to 0.056. Figure 9(b) depicts the current distributions in the employed resonator at the corresponding resonant frequencies. It is observed that increasing the offset distance enhances the coupling between the folded components and adjacent edges, shortening the current paths and producing a red-shift of the magnetic resonance. Moreover, benefitting from the miniaturized metasurface periodicity, the constitutive parameters ε_t and μ_n exhibit angular stability, as shown in Figures 8(c) and 9(d). In addition, a slight fluctuation of the constitutive parameter μ_n from its theoretical target is observed at large incidence angles. Due to the term $\sin^2\theta/\mu_t\mu_n$, this fluctuation is amplified at large incidence angles, resulting in a mismatch between the simulation and theoretical analysis, as illustrated in Figure 6(c). Nevertheless, this mismatch has a negligible impact on the angular bandwidth and selectivity of the designed metasurface.

It is noteworthy that designing the metasurface to operate in the non-resonant region effectively ensures that the tangential permeability remains unaffected by the anti-resonance phenomena near the resonant frequency in periodic metasurfaces. Furthermore, due to the absence of loop currents along the normal direction, the tangential relative permeability μ_t of the metasurface remains unity, which is consistent with the desired condition (15).

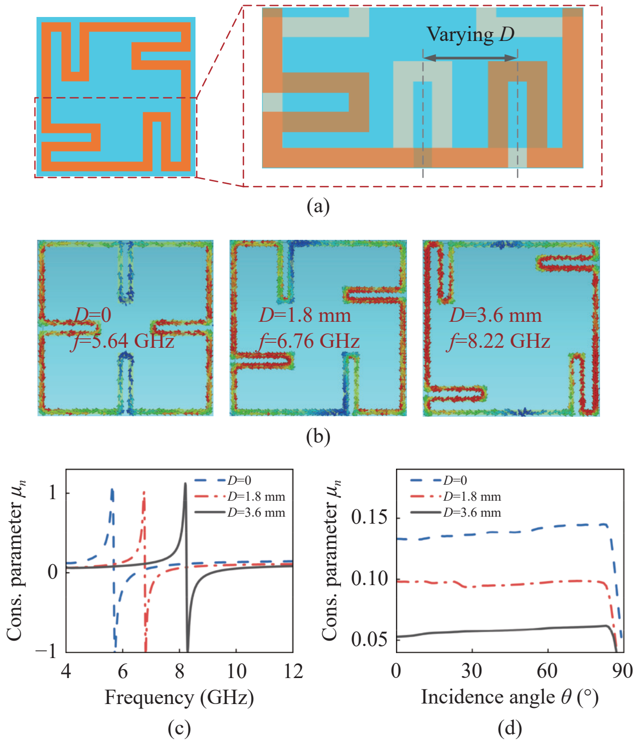

Figure 9 Influence of offset distance D on the constitutive parameter μ_n: (a) Schematic diagram of the variation in offset distance; (b) Frequency response and (c) Angular response at 10 GHz of the parameter μ_n with variation of D.

3. Experimental validation

To experimentally validate the proposed angular metasurface design methodology, a prototype was fabricated using standard printed circuit board (PCB) technology. As depicted in Figure 10(a), the sample consists of 30×30 unit cells and has overall dimensions of 300 mm×300 mm×0.4 mm. Figure 10(b) illustrates the impact of the PCB fabrication tolerance (±0.01 mm) on the angular response, with variations in two key structural parameters: D and L_{in}. The results indicate that deviations in D induce slight shifts in the angular response, while those in L_{in} have a negligible influence. This discrepancy stems from their respective roles in tailoring the constitutive parameters: D modulates the normal relative permeability μ_n with an extremely small target value of 0.057, making the response more sensitive to dimensional variations. In contrast, L_{in} governs the tangential relative permittivity ε_t, with a relatively large value of 1, which is more robust against fabrication errors. Overall, the metasurface maintains stable angular performance, including bandwidth and selectivity, within fabrication tolerances, demonstrating the robustness of the proposed design.

Subsequently, the fabricated prototype was measured in a microwave anechoic chamber using the free-space method [17]. As shown in Figure 10(a), the prototype was

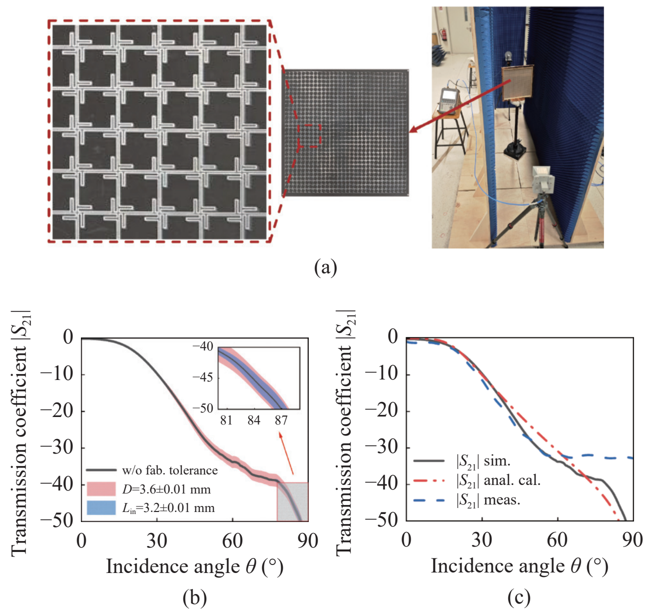

Figure 10 Fabrication and experiment: (a) Photographs of the fabricated angular metasurface and its experimental setup; (b) Fabrication tolerance on the metasurface angular performance considering two key parameters: D and L_{in}; (c) Measured angular spectrum of the fabricated prototype, together with simulated and calculated results.

mounted on a turntable, while the transmitting and receiving horn antennas were placed on either side and connected to a two-port vector network analyzer (ZNH18) via coaxial cables. By rotating the turntable, the angular transmission spectrum was measured across various incidence angles. The time-domain gating technique was applied to eliminate environmental interference, and the measured results were then normalized to the reference case of an air window, yielding the resulting angular spectrum of the prototype. Figure 10(c) illustrates that the fabricated prototype exhibits an angular response with a cutoff angle of 19.2° and a rejection angle of 29.1°, closely matching the simulated results. The slight discrepancy between the two is attributed to surface unevenness caused by the flexibility of the ultrathin prototype. In addition, larger deviations at higher incidence angles are mainly due to the limited dynamic range of the vector network analyzer, which restricts its sensitivity to low transmission levels.

IV. Discussion

1. Versatility of the proposed design paradigm

Based on the proposed constitutive-parameter-driven design paradigm, the constitutive parameters required to achieve a specific angular performance can be analytically derived and physically realized through appropriate electrical/magnetic resonators. Notably, these parameters are frequency-independent, making the design paradigm intrinsically versatile in frequency. To demonstrate its frequency and angular versatility, a metasurface was designed to operate at 12.5 GHz with an angular bandwidth and selectivity of 30° and 1.6. The required constitutive parameters were derived as $\varepsilon_t = \mu_t = 1$, $\mu_n = 0.111$, and $h = 0.3$ mm. The unit cell maintains the same topology as in Figure 6 but with different dimensions ($P = 8.0$ mm, $L_s = 7.6$ mm, $L_{\text{in}} = 3.0$ mm, $D = 3.0$ mm, $W_{\text{in}} = 0.5$ mm, and $W_s = 0.24$ mm). The resulting metasurface exhibits an angular bandwidth of 30.1° and an angular selectivity of 1.63 at 12.5 GHz, which are in close agreement with the analytically calculated values obtained from (2), (8), and (15), as illustrated in Figure 11(a). This consistency is attributed to the close alignment between the physically achieved and the theoretically derived constitutive parameters, i.e., ε_t and μ_n, over a broad angular range, as depicted in Figure 11(b). These results confirm both the effectiveness of the proposed paradigm and its versatility across different frequency and angular regimes.

Admittedly, only at a single frequency (10 GHz) and under TE polarization, the physically realized metasurface achieves the desired angular performance. However, since the constitutive parameter conditions are derived independently of frequency, the proposed design paradigm can be extended to a broader frequency band, provided that these conditions are fulfilled across a wide frequency range. Specifically, since the free-space wavenumber k_0 increases with increasing frequency, maintaining a constant phase factor $k_0 h \mu_t$ within a fixed-thickness metasurface and satisfying the condition $\varepsilon_t = \mu_t$ across a broad frequency band would require both parameters ε_t and μ_t to decrease with increasing frequency. This contradicts the typical positive dispersion behavior of conventional resonant modes, in which both constitutive parameters generally increase with increasing frequency, thereby constraining broadband realization. Encouragingly, our previous work has demonstrated that anti-resonant modes excited within metasurfaces can induce opposite dispersion [54], offering a potential pathway to achieving a broadband response. Moreover, according to the reciprocity principle, the angular response can be extended from TE to TM polarization by interchanging the permittivity and permeability in the constitutive parameter conditions. In particular, this involves transforming the condition involving $\varepsilon_t = \mu_t$, $\mu_t \mu_n$, and $k_0 h \mu_t$ into the corresponding expressions $\mu_t = \varepsilon_t$, $\varepsilon_t \varepsilon_n$, and $k_0 h \varepsilon_t$. Therefore, by maintaining the condition $\varepsilon_t = \mu_t$ and exciting electric resonances in the normal direction to tune the normal relative permittivity ε_n, the desired angular response under TM polarization can be achieved. Based on these strategies, angular metasurfaces with broadband and multi-polarization properties can be further explored.

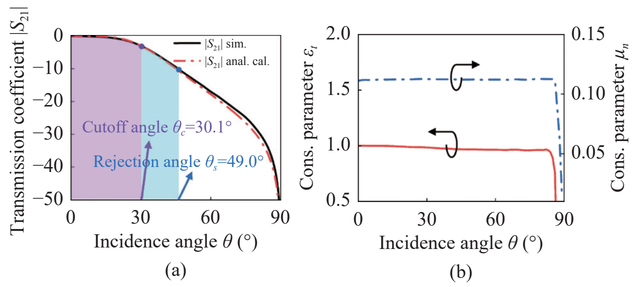

Figure 11 Performance and parameters of the angular metasurface with different angular performance and operating frequency: (a) Simulated and analytically calculated angular performance of the metasurface with an angular bandwidth of 30° and an angular selectivity of 1.6, and (b) Its constitutive parameters ε_t and μ_n in the angular domain.

2. Extension to highpass and bandpass transmissive angular metasurfaces

The proposed constitutive-parameter-driven design paradigm is primarily developed for lowpass transmissive angular metasurfaces, in which perfect transmission occurs at normal incidence and gradually decreases with increasing incidence angle. This design paradigm can be further extended to highpass and bandpass cases by modifying the transmission conditions. For highpass transmissive angular metasurfaces, the design objective is converted to achieve perfect transmission at $\theta = 90°$, i.e., $|S_{21}|_{\theta=90°} = 1$, with minimal transmission at normal incidence. This condition requires the interface reflectivity $r_L|_{\theta=90°} = 0$ and leads to a constutive parameter constraint $\varepsilon_t/\mu_t = 1/\mu_t\mu_n$. For bandpass transmissive angular metasurfaces, the design objective is to allow perfect transmission at a specific target angle θ_d, i.e., $|S_{21}|_{\theta=\theta_d} = 1$, while suppressing transmission at angles on both sides of θ_d. This condition can be fulfilled by realizing the Brewster effect at the target angle, which

Electromagnetic Science

leads to $\sin\theta_d = \sqrt{(\varepsilon_t-\mu_t)/(1/\mu_n-\mu_t)}$ [45]. Based on the above conditions, and combined with the resonator-based method used in this work for tuning the constitutive parameters, the proposed design paradigm can be naturally extended to the highpass and bandpass cases. This approach is complementary to the method of mechanically rotating the metasurface to tune its operating angle and holds significant potential for broadening the application scenarios of angular metasurfaces.

3. Enhanced angular selectivity via multilayer structures

It is worth noting that the theoretical derivations in this work are based on the assumption that the constitutive parameters of the metasurface are non-dispersive with respect to the incidence angle, which inherently imposes theoretical boundaries on the angular selectivity of single-layer metasurfaces. Our previous studies have shown that stacking multilayer metasurfaces with quarter-wavelength spacing and appropriate bandwidth allocation can achieve sharp frequency selectivity while suppressing interlayer coupling [52]. This strategy can potentially be applied to angular metasurfaces to enhance angular selectivity. Specifically, by stacking multiple metasurfaces with tailored angular bandwidths, one can emulate classical filter designs such as Butterworth or Chebyshev filters, thereby achieving angular responses with features such as maximally flat passbands or steeper angular roll-off. To validate this strategy, we constructed a bilayer structure by stacking two identical metasurfaces as shown in Figure 6, emulating a second-order Butterworth filter, as depicted in Figure 12(a). As expected, the simulation results in Figure 12(b) demonstrate that the bilayer metasurface enhances angular selectivity compared to the single-layer case, although the angular bandwidth becomes narrower. This behavior is analogous to that of a second-order Butterworth filter in the frequency domain, confirming the feasibility of enhancing angular selectivity through stacking multilayer metasurfaces. In addition, a flatter angular response, i.e., lower angular selectivity, can be achieved by employing metasurfaces with angularly dispersive constitutive parameters.

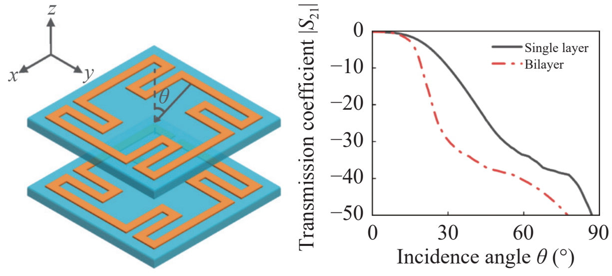

Figure 12 Multilayer structures for higher angular selectivity: (a) The schematic diagram of an angular metasurface with a bilayer configuration; (b) The angular response of the bilayer angular metasurface and that of single layer case.

V. Conclusion

In summary, this work proposes a universal "angular response–constitutive parameter–metasurface structure" design paradigm for angular metasurfaces. Leveraging the constitutive parameters, the desired angular response can be directly linked to the physical metasurfaces. This paradigm eliminates the trial-and-error process for structure selection inherent in conventional approaches, fundamentally removing the critical reliance on extensive and non-generalizable numerical simulations while retaining only minor simulations for final structural optimization. As experimental validation, folded loop resonators are employed in a practical metasurface to tailor the required constitutive parameters for the desired response, achieving an angular bandwidth of 19.2° and an angular selectivity of 1.51, which are in good agreement with the predefined results. Overall, this work provides a concise and time-efficient framework that enables flexible angular functionalities of EM waves, such as beam shaping and spatial-wave computing, with promising applications including anti-interference communications, image edge detection, and multi-view holography.

Acknowledgements

This work was supported by the National Research Foundation, Singapore, and Infocomm Media Development Authority under its Future Communications Research & Development Programme (Grant No. FCP-NTU-RG-2024-025), the MOE Tier 2 (Grant No. MOE-T2EP50124-0032), A*STAR (Agency for Science, Technology and Research) Singapore (Grant No. M22L1b0110), the National Natural Science Foundation of China (NSFC) (Grant No. U22B 2016), and the National Key Research and Development Program of China (Grant No. 2021YFA0716601).

Appendix A. Transmission Coefficients of Metasurface with Zero Constitutive Parameters

1. ENZ metasurfaces

For ENZ metasurfaces, only the tangential relative permittivity is approximately zero, i.e., $\varepsilon_t = 0$ and $\mu_t \neq 0$. In this regard, the interface reflection r in (3) is rewritten as follows:

$$r_E = \frac{\cos\theta - \sqrt{-\dfrac{\sin^2\theta}{\mu_t\mu_n}}}{\cos\theta + \sqrt{-\dfrac{\sin^2\theta}{\mu_t\mu_n}}} = \frac{\cos\theta - \mathrm{j}A_E}{\cos\theta + \mathrm{j}A_E} \tag{A-1}$$

where $A_E = \sqrt{\sin^2\theta/\mu_t\mu_n}$. Based on (4), the phase change φ_E in ENZ metasurfaces is given by

$$\varphi_E = k_0 h\mu_t\sqrt{-\sin^2\theta/\mu_t\mu_n} = \mathrm{j}k_c\mu_t A_E \tag{A-2}$$

where $k_c = k_0 h$. Substituting (A-1) and (A-2) into (2), the transmission coefficient becomes

$$\left|S_{21}^{E}\right| = \left|\frac{(1-r_E^2)\mathrm{e}^{-\mathrm{j}\varphi_E}}{1-r_E^2\mathrm{e}^{-\mathrm{j}2\varphi_E}}\right| = \left|\frac{4\mathrm{e}^{k_c\mu_t A_E}}{\frac{\cos^2\theta - A_E^2}{A_E\cos\theta}(1-\mathrm{e}^{2k_c\mu_t A_E}) + 2\mathrm{j}(1+\mathrm{e}^{2k_c\mu_t A_E})}\right| \tag{A-3}$$

It is apparent that A_E is approximately zero as the incidence angle θ approaches zero, and according to the Taylor expansion formula, we have

$$1-\mathrm{e}^{2k_c\mu_t A_E} = -2k_c\mu_t A_E - o(2k_c\mu_t A_E) \tag{A-4}$$

where $o(\cdot)$ represents the higher-order infinitesimal terms in a Taylor expansion formula.

Substituting (A-4) into (A-3), the transmission coefficient can be simplified as follows:

$$\begin{aligned}\left|S_{21}^{E}\right|_{\theta=0} &= \left|\frac{4\mathrm{e}^{k_c\mu_t A_E}}{\frac{\cos^2\theta - A_E^2}{A_E\cos\theta}(1-\mathrm{e}^{2k_c\mu_t A_E}) + 2\mathrm{j}(1+\mathrm{e}^{2k_c\mu_t A_E})}\right| \\ &= \left|\frac{4}{-2k_c\mu_t + 4\mathrm{j}}\right| = \frac{2}{\sqrt{4+(k_c\mu_t)^2}}\end{aligned} \tag{A-5}$$

Thus, the transmission coefficient of ENZ metasurfaces under normal incidence is consistently less than unity and depends on the parameter $k_c\mu_t$.

2. MNZ metasurfaces

For MNZ metasurfaces, only the tangential relative permeability approaches zero, i.e., $\mu_t = 0$ and $\varepsilon_t \neq 0$. Under this condition, the interface reflection r in (3) is rewritten as

$$r_M = \frac{\cos\theta - \sqrt{\frac{\varepsilon_t}{\mu_t} - \frac{\sin^2\theta}{\mu_t\mu_n}}}{\cos\theta + \sqrt{\frac{\varepsilon_t}{\mu_t} - \frac{\sin^2\theta}{\mu_t\mu_n}}} = \frac{\sqrt{\mu_t}\cos\theta - \sqrt{\varepsilon_t - \frac{\sin^2\theta}{\mu_n}}}{\sqrt{\mu_t}\cos\theta + \sqrt{\varepsilon_t - \frac{\sin^2\theta}{\mu_n}}} \tag{A-6}$$

Here, for the sake of subsequent analysis, the parameter μ_t is retained in the interface reflection r_M. Under normal incidence, the expression $\varepsilon_t - \sin^2\theta/\mu_n$ remains positive, thus we define $A_M = \sqrt{\varepsilon_t - \sin^2\theta/\mu_n}$, and (A-6) can be simplified as follows:

$$r_M = \frac{\sqrt{\mu_t}\cos\theta - A_M}{\sqrt{\mu_t}\cos\theta + A_M} \tag{A-7}$$

According to (4), the phase change φ_M in an MNZ metasurface can be written as follows:

$$\varphi_M = k_0 h\mu_t\sqrt{\frac{\varepsilon_t}{\mu_t} - \frac{\sin^2\theta}{\mu_t\mu_n}} = k_c\sqrt{\mu_t}A_M \tag{A-8}$$

Substituting (A-7) and (A-8) into (2), the transmission coefficient can be expressed as follows:

$$\begin{aligned}\left|S_{21}^{M}\right| &= \left|\frac{(1-r_M^2)\mathrm{e}^{-\mathrm{j}\varphi_M}}{1-r_M^2\mathrm{e}^{-\mathrm{j}2\varphi_M}}\right| = \left|\frac{(1-r_M^2)\mathrm{e}^{-\mathrm{j}k_c\sqrt{\mu_t}A_M}}{1-r_M^2\mathrm{e}^{-\mathrm{j}2k_c\sqrt{\mu_t}A_M}}\right| \\ &= \left|\frac{4\mathrm{e}^{-\mathrm{j}k_c\sqrt{\mu_t}A_M}}{\frac{\mu_t\cos^2\theta + A_M^2}{\sqrt{\mu_t}A_M\cos\theta}(1-\mathrm{e}^{-\mathrm{j}2k_c\sqrt{\mu_t}A_M}) + 2\mathrm{j}(1+\mathrm{e}^{-\mathrm{j}2k_c\sqrt{\mu_t}A_M})}\right|\end{aligned} \tag{A-9}$$

When the tangential relative permeability μ_t approaches zero, according to the Taylor expansion formula, we have

$$1-\mathrm{e}^{-\mathrm{j}2k_c\sqrt{\mu_t}A_M} = \mathrm{j}2k_c\sqrt{\mu_t}A_M - o(-\mathrm{j}2k_c\sqrt{\mu_t}A_M) \tag{A-10}$$

Substituting (A-10) into (A-9), the transmission coefficient under normal incidence can be simplified as follows:

$$\begin{aligned}\left|S_{21}^{M}\right|_{\theta=0} &= \left|\frac{4\mathrm{e}^{-\mathrm{j}k_c\sqrt{\mu_t}A_M}}{\frac{\mu_t\cos^2\theta + A_M^2}{\sqrt{\mu_t}A_M\cos\theta}(1-\mathrm{e}^{-\mathrm{j}2k_c\sqrt{\mu_t}A_M}) + 2\mathrm{j}(1+\mathrm{e}^{-\mathrm{j}2k_c\sqrt{\mu_t}A_M})}\right| \\ &= \left|\frac{4}{-\mathrm{j}2k_cA_M^2 + 4}\right| = \frac{2}{\sqrt{4+(k_c\varepsilon_t)^2}}\end{aligned} \tag{A-11}$$

Hence, under normal incidence, the transmission coefficient of MNZ metasurfaces is consistently less than unity and is closely related to the parameter $k_c\varepsilon_t$.

3. EMNZ metasurfaces

For EMNZ metasurfaces, both the tangential relative permittivity and permeability are approximately zero, i.e., $\varepsilon_t = \mu_t = 0$. In this way, the interface reflection r in (3) is rewritten as follows:

$$\begin{aligned}r_{\mathrm{EM}} &= \frac{\cos\theta - \sqrt{\frac{\varepsilon_t}{\mu_t} - \frac{\sin^2\theta}{\mu_t\mu_n}}}{\cos\theta + \sqrt{\frac{\varepsilon_t}{\mu_t} - \frac{\sin^2\theta}{\mu_t\mu_n}}} = \frac{\sqrt{\mu_t}\cos\theta - \sqrt{\varepsilon_t - \frac{\sin^2\theta}{\mu_n}}}{\sqrt{\mu_t}\cos\theta + \sqrt{\varepsilon_t - \frac{\sin^2\theta}{\mu_n}}} \\ &= \frac{\sqrt{\mu_t}\cos\theta - \sqrt{-\frac{\sin^2\theta}{\mu_n}}}{\sqrt{\mu_t}\cos\theta + \sqrt{-\frac{\sin^2\theta}{\mu_n}}} = \frac{\sqrt{\mu_t}\cos\theta - \mathrm{j}A_{\mathrm{EM}}}{\sqrt{\mu_t}\cos\theta + \mathrm{j}A_{\mathrm{EM}}}\end{aligned} \tag{A-12}$$

where $A_{\mathrm{EM}} = \sqrt{\sin^2\theta/\mu_n}$. According to (4), the phase change φ_{EM} in an EMNZ metasurface is expressed as follows:

$$\varphi_{\mathrm{EM}} = k_0 h\sqrt{\mu_t}\sqrt{-\frac{\sin^2\theta}{\mu_t\mu_n}} = \mathrm{j}k_c\sqrt{\mu_t}A_{\mathrm{EM}} \tag{A-13}$$

Substituting (A-12) and (A-13) into (2), the transmission coefficient can be rewritten as follows:

$$\begin{aligned}\left|S_{21}^{\mathrm{EM}}\right| &= \left|\frac{(1-r_{\mathrm{EM}}^2)\mathrm{e}^{-\mathrm{j}\varphi_{\mathrm{EM}}}}{1-r_{\mathrm{EM}}^2\mathrm{e}^{-\mathrm{j}2\varphi_{\mathrm{EM}}}}\right| \\ &= \left|\frac{4\mathrm{e}^{k_c\sqrt{\mu_t}A_{\mathrm{EM}}}}{-\mathrm{j}\frac{\mu_t\cos^2\theta - A_{\mathrm{EM}}^2}{\sqrt{\mu_t}A_{\mathrm{EM}}\cos\theta}(1-\mathrm{e}^{2k_c\sqrt{\mu_t}A_{\mathrm{EM}}}) + 2(1+\mathrm{e}^{2k_c\sqrt{\mu_t}A_{\mathrm{EM}}})}\right|\end{aligned} \tag{A-14}$$

where A_{EM} is approximately zero as the incidence angle θ approaches zero, and according to the Taylor expansion formula, we obtain

$$1-\mathrm{e}^{2k_c\sqrt{\mu_t}A_{\mathrm{EM}}} = -2k_c\sqrt{\mu_t}A_{\mathrm{EM}} - o(2k_c\sqrt{\mu_t}A_{\mathrm{EM}}) \tag{A-15}$$

Substituting (A-15) into (A-14), the transmission coefficient can be simplified as follows:

$$\begin{aligned}\left|S_{21}^{\mathrm{EM}}\right| &= \left|\frac{4\mathrm{e}^{k_c\sqrt{\mu_t}A_{\mathrm{EM}}}}{-\mathrm{j}\frac{\mu_t\cos^2\theta - A_{\mathrm{EM}}^2}{\sqrt{\mu_t}A_{\mathrm{EM}}\cos\theta}(1-\mathrm{e}^{2k_c\sqrt{\mu_t}A_{\mathrm{EM}}}) + 2(1+\mathrm{e}^{2k_c\sqrt{\mu_t}A_{\mathrm{EM}}})}\right| \\ &= \left|\frac{4}{4+\mathrm{j}\frac{2k_c\sin^2\theta}{\mu_n\cos\theta}}\right|\end{aligned} \tag{A-16}$$

Thus, for the case of normal incidence, the transmission coefficient is consistently unity, that is,

$$\left|S_{21}^{\mathrm{EM}}\right|_{\theta=0}=\left|\frac{4}{4+\mathrm{j}\dfrac{2k_c\sin^2\theta}{\mu_n\cos\theta}}\right|=1 \tag{A-17}$$

Therefore, based on (A-5), (A-11), and (A-17), only EMNZ metasurfaces exhibit perfect transmission ($|S_{21}|=1$) under normal incidence, while ENZ and MNZ metasurfaces can only asymptotically approach unity unless both the tangential relative permittivity and permeability simultaneously approach zero, in which case they are indistinguishable from EMNZ metasurfaces.

Appendix B. Derivation of Critical Phase Factor

At the critical condition where the cutoff angle contour first intersects the real–imaginary boundary of the root term $\sqrt{1-\sin^2\theta/\mu_t\mu_n}$, the cutoff angle and the permeability factor of the metasurface lie precisely on this boundary, satisfying $\sin^2\theta_c=\mu_t\mu_n$. Under this condition, and according to (8), the interface reflectivity becomes $r_L=1$, while the phase change is $\varphi_L=0$. Therefore, the transmission coefficient of the metasurface can be expressed as follows:

$$\begin{aligned}|S_{21}|&=\left|\frac{(1-r_L^2)\mathrm{e}^{-\mathrm{j}\varphi_L}}{1-r_L^2\mathrm{e}^{-\mathrm{j}2\varphi_L}}\right|=\left|\frac{(1+r_L)(1-r_L)}{(1+r_L\mathrm{e}^{-\mathrm{j}\varphi_L})(1-r_L\mathrm{e}^{-\mathrm{j}\varphi_L})}\right|=\left|\frac{1-r_L}{1-r_L\mathrm{e}^{-\mathrm{j}\varphi_L}}\right|\\&=\left|\frac{\cos\theta_c+\sqrt{1-\dfrac{\sin^2\theta_c}{\mu_t\mu_n}}-\cos\theta_c+\sqrt{1-\dfrac{\sin^2\theta_c}{\mu_t\mu_n}}}{\cos\theta_c+\sqrt{1-\dfrac{\sin^2\theta_c}{\mu_t\mu_n}}-(\cos\theta_c-\sqrt{1-\dfrac{\sin^2\theta_c}{\mu_t\mu_n}})\mathrm{e}^{-\mathrm{j}\varphi_L}}\right|\\&=\left|\frac{2\sqrt{1-\dfrac{\sin^2\theta_c}{\mu_t\mu_n}}}{\cos\theta_c(1-\mathrm{e}^{-\mathrm{j}\varphi_L})+\sqrt{1-\dfrac{\sin^2\theta_c}{\mu_t\mu_n}}(1+\mathrm{e}^{-\mathrm{j}\varphi_L})}\right|\\&=\left|\frac{2}{\dfrac{\cos\theta_c}{\sqrt{1-\dfrac{\sin^2\theta_c}{\mu_t\mu_n}}}(1-\mathrm{e}^{-\mathrm{j}\varphi_L})+(1+\mathrm{e}^{-\mathrm{j}\varphi_L})}\right|\end{aligned} \tag{B-1}$$

where φ_L is approximately zero. In this case, according to the Taylor expansion formula, the term $1-\mathrm{e}^{-\mathrm{j}\varphi_L}$ tends to zero and can be equivalently expressed as:

$$1-\mathrm{e}^{-\mathrm{j}\varphi_L}=\mathrm{j}\varphi_L=\mathrm{j}k_0h\mu_t\sqrt{1-\frac{\sin^2\theta_c}{\mu_t\mu_n}} \tag{B-2}$$

while the term $1+\mathrm{e}^{-\mathrm{j}\varphi_L}=2$. Then, using these relationships, the transmission coefficient can be rewritten as follows:

$$\begin{aligned}|S_{21}|&=\left|\frac{2}{\dfrac{\cos\theta_c}{\sqrt{1-\dfrac{\sin^2\theta_c}{\mu_t\mu_n}}}\mathrm{j}k_0h\mu_t\sqrt{1-\dfrac{\sin^2\theta_c}{\mu_t\mu_n}}+2}\right|\\&=\left|\frac{2}{\mathrm{j}k_0h\mu_t\cos\theta_c+2}\right|=\frac{2}{\sqrt{4+(k_0h\mu_t\cos\theta_c)^2}}\end{aligned} \tag{B-3}$$

Since, under critical conditions, the cutoff angle and the permeability factor both approach zero, i.e., $\theta_c\to0$, $\mu_t\mu_n\to0$, the above expression reduces to

$$|S_{21}|=\frac{2}{\sqrt{4+(k_0h\mu_t)^2}}=-3\ \mathrm{dB} \tag{B-4}$$

Consequently, the corresponding phase factor $k_0h\mu_t$ for this critical state is 2. This value serves as the threshold determining whether the cutoff angle contour intersects the real-imaginary boundary of the root term $\sqrt{1-\sin^2\theta/\mu_t\mu_n}$.

Appendix C. Derivation of Cutoff Angle

1. Phase factor less than or equal to 2

When the phase factor satisfies $k_0h\mu_t\le2$, the cutoff angle contour lies entirely within the region where the root term $\sqrt{1-\sin^2\theta_c/\mu_t\mu_n}$ is imaginary. In this case, the interface reflectivity r_L and the phase change φ_L can be expressed as

$$r_L=\frac{\cos\theta_c-\mathrm{j}A_N}{\cos\theta_c+\mathrm{j}A_N}\quad\text{and}\quad\varphi_L=\mathrm{j}k_0h\mu_tA_N \tag{C-1}$$

respectively, where $A_N=\sqrt{\sin^2\theta_c/\mu_t\mu_n-1}$. Substituting (C-1) into (9) yields

$$\left|\frac{\cos\theta_c+\mathrm{j}A_N}{\cos\theta_c-\mathrm{j}A_N}-\frac{\cos\theta_c-\mathrm{j}A_N}{\cos\theta_c+\mathrm{j}A_N}\right|=\left|\mathrm{e}^{-k_0h\mu_tA_N}-\mathrm{e}^{k_0h\mu_tA_N}\right| \tag{C-2}$$

where $\cos\theta_c$, A_N, and $k_0h\mu_t$ are all positive. Therefore (C-2) can be simplified as follows:

$$\frac{4A_N\cos\theta_c}{\cos^2\theta_c+A_N^2}=\mathrm{e}^{k_0h\mu_tA_N}-\mathrm{e}^{-k_0h\mu_tA_N} \tag{C-3}$$

Then, the solution can be rewritten as follows:

$$\mathrm{e}^{k_0h\mu_tA_N}=\frac{1+\sqrt{1+F_N^2}}{F_N} \tag{C-4}$$

where $F_N=(\cos^2\theta_c+A_N^2)/(2A_N\cos\theta_c)$. Thus, the analytical relationship among the cutoff angle θ_c, the phase factor $k_0h\mu_t$, and the permeability factor $\mu_t\mu_n$ when $k_0h\mu_t\le2$ is

$$k_0h\mu_t=\frac{1}{A_N}\ln\frac{1+\sqrt{1+F_N^2}}{F_N} \tag{C-5}$$

2. Phase factor larger than 2

When the phase factor satisfies $k_0h\mu_t>2$, the cutoff angle contour intersects the real-imaginary boundary of the root term $\sqrt{1-\sin^2\theta/\mu_t\mu_n}$. At this intersection, the cutoff angle and permeability factor satisfy $\sin^2\theta_c=\mu_t\mu_n$ and the transmission coefficient is $|S_{21}|=-3\ \mathrm{dB}$. According to (B-3), we have

$$\begin{aligned}|S_{21}|&=\frac{2}{\sqrt{4+(k_0h\mu_t\cos\theta_c)^2}}=\frac{2}{\sqrt{4+(k_0h\mu_t)^2(1-\sin^2\theta_c)}}\\&=\frac{2}{\sqrt{4+(k_0h\mu_t)^2(1-\mu_t\mu_n)}}=-3\ \mathrm{dB}\end{aligned} \tag{C-6}$$

from which the analytical relationship between the permeability factor and the phase factor at the intersection can be derived as follows:

$$\mu_t\mu_n = 1 - \frac{4}{(k_0 h\mu_t)^2} \tag{C-7}$$

As demonstrated in Figure 2, when $k_0 h\mu_t > 2$ and $0 < \mu_t\mu_n < 1 - 4/(k_0 h\mu_t)^2$, the root term $\sqrt{1-\sin^2\theta_c/\mu_t\mu_n}$ on the cutoff angle contour is real. In this case, the interface reflectivity r_L and the phase change φ_L can be expressed as

$$r_L = \frac{\cos\theta_c - A_P}{\cos\theta_c + A_P} \quad \text{and} \quad \varphi_L = k_0 h\mu_t A_P \tag{C-8}$$

respectively, where $A_P = \sqrt{1-\sin^2\theta_c/\mu_t\mu_n}$. Substituting (C-8) into (9) yields

$$\left|\frac{\cos\theta_c + A_P}{\cos\theta_c - A_P} - \frac{\cos\theta_c - A_P}{\cos\theta_c + A_P}\right| = \left|e^{jk_0 h\mu_t A_P} - e^{-jk_0 h\mu_t A_P}\right| \tag{C-9}$$

where $\cos\theta_c$, A_P, and $k_0 h\mu_t$ are all positive. Therefore (C-9) can be simplified as follows:

$$\frac{2A_P\cos\theta_c}{\cos^2\theta_c - A_P^2} = \sin(k_0 h\mu_t A_P) \tag{C-10}$$

Then, the analytical relationship among the cutoff angle θ_c, the phase factor $k_0 h\mu_t$, and the permeability factor $\mu_t\mu_n$ can be obtained as follows:

$$k_0 h\mu_t = \frac{1}{A_P}\sin^{-1}(F_P) \tag{C-11}$$

in which $F_P = 2A_P\cos\theta_c/(\cos^2\theta_c - A_P^2)$. For the case of $k_0 h\mu_t > 2$ and $1 - 4/(k_0 h\mu_t)^2 < \mu_t\mu_n < 1$, the root term $\sqrt{1-\sin^2\theta_c/\mu_t\mu_n}$ on the cutoff angle contour becomes imaginary again, and the analytical relationship among the cutoff angle θ_c, the phase factor $k_0 h\mu_t$, and the permeability factor $\mu_t\mu_n$ reverts to the same form as in (C-5). Consequently, when $k_0 h\mu_t > 2$, their analytical relationship can be summarized as follows:

$$\begin{cases} k_0 h\mu_t = \dfrac{1}{A_P}\sin^{-1}(F_P), & 0 < \mu_t\mu_n \le 1 - \dfrac{4}{(k_0 h\mu_t)^2} \\ k_0 h\mu_t = \dfrac{1}{A_N}\ln\dfrac{1+\sqrt{1+F_N^2}}{F_N}, & 1 - \dfrac{4}{(k_0 h\mu_t)^2} < \mu_t\mu_n < 1 \end{cases} \tag{C-12}$$

References

[1] R. A. Shelby, D. R. Smith, and S. Schultz, "Experimental verification of a negative index of refraction," *Science*, vol. 292, no. 5514, pp. 77–79, 2001.

[2] N. F. Yu, P. Genevet, M. A. Kats, *et al*., "Light propagation with phase discontinuities: Generalized laws of reflection and refraction," *Science*, vol. 334, no. 6054, pp. 333–337, 2011.

[3] J. C. Zhang, G. B. Wu, M. K. Chen, *et al*., "Electromagnetic wave tailoring: From one dimension to multiple dimensions," *Electromagnetic Science*, vol. 1, no. 3, article no. 0030131, 2023.

[4] B. Zhang, Z. N. Chen, Y. C. Zhou, *et al*., "Improving radiation pattern roundness of henge-like metaring-loaded monopoles above a finite ground for MIMO systems," *Electromagnetic Science*, vol. 2, no. 2, article no. 0060182, 2024.

[5] Q. H. Lv, C. Jin, B. C. Zhang, *et al*., "Hybrid absorptive-diffusive frequency selective radome," *IEEE Transactions on Antennas and Propagation*, vol. 69, no. 6, pp. 3312–3321, 2021.

[6] N. A. Rubin, P. Chevalier, M. Juhl, *et al*., "Imaging polarimetry through metasurface polarization gratings," *Optics Express*, vol. 30, no. 6, pp. 9389–9412, 2022.

[7] Q. B. Fan, W. Z. Xu, X. M. Hu, *et al*., "Disordered metasurface enabled single-shot full-Stokes polarization imaging leveraging weak dichroism," *Nature Communications*, vol. 14, no. 1, article no. 7180, 2023.

[8] A. Zaidi, N. A. Rubin, M. L. Meretska, *et al*., "Metasurface-enabled single-shot and complete Mueller matrix imaging," *Nature Photonics*, vol. 18, no. 7, pp. 704–712, 2024.

[9] X. Jiang, H. Chen, Z. Y. Li, *et al*., "All-dielectric metalens for terahertz wave imaging," *Optics Express*, vol. 26, no. 11, pp. 14132–14142, 2018.

[10] A. A. Fathnan, M. K. Liu, and D. A. Powell, "Achromatic Huygens' metalenses with deeply subwavelength thickness," *Advanced Optical Materials*, vol. 8, no. 22, article no. 2000754, 2020.

[11] K. Chen, Y. J. Feng, F. Monticone, *et al*., "A reconfigurable active Huygens' metalens," *Advanced Materials*, vol. 29, no. 17, article no. 1606422, 2017.

[12] J. X. Zhou, S. K. Liu, H. L. Qian, *et al*., "Metasurface enabled quantum edge detection," *Science Advances*, vol. 6, no. 51, article no. eabc4385, 2020.

[13] R. S. Tanuwijaya, H. Liang, J. W. Xi, *et al*., "Metasurface for programmable quantum algorithms with classical and quantum light," *Nanophotonics*, vol. 13, no. 6, pp. 927–936, 2024.

[14] M. B. Yan, J. F. Wang, H. Ma, *et al*., "A tri-band, highly selective, bandpass FSS using cascaded multilayer loop arrays," *IEEE Transactions on Antennas and Propagation*, vol. 64, no. 5, pp. 2046–2049, 2016.

[15] Q. H. Lv, C. Jin, B. C. Zhang, *et al*., "Wide-passband dual-polarized elliptic frequency selective surface," *IEEE Access*, vol. 7, pp. 55833–55840, 2019.

[16] Y. J. Zhang, Y. Li, W. Q. Zhang, *et al*., "Omnidirectional antenna diversity system for high-speed onboard communication," *Engineering*, vol. 11, pp. 72–79, 2022.

[17] C. Jin, Q. H. Lv, and R. Mittra, "Dual-polarized frequency-selective surface with two transmission zeros based on cascaded ground apertured annular ring resonators," *IEEE Transactions on Antennas and Propagation*, vol. 66, no. 8, pp. 4077–4085, 2018.

[18] Y. J. Zhang and Y. Li, "Wideband microstrip antenna in small volume without using fundamental mode," *Electromagnetic Science*, vol. 1, no. 2, article no. 0020073, 2023.

[19] H. Jiang, Z. Zhang, Y. H. Zhang, *et al*., "Millimeter-wave quasi-elliptical bandpass FSS using macro cells," *IEEE Transactions on Antennas and Propagation*, vol. 72, no. 9, pp. 7371–7376, 2024.

[20] X. X. Guo, Y. Luo, Z. N. Chen, *et al*., "Interferometric phase transmitarray for spatial power combining to enhance EIRP of millimeter-wave transmitters," *IEEE Transactions on Antennas and Propagation*, vol. 70, no. 11, pp. 10485–10493, 2022.

[21] A. Papathanasopoulos and Y. Rahmat-Samii, "Transmitarray antenna for conical beam scanning," *IEEE Transactions on Antennas and Propagation*, vol. 70, no. 11, pp. 11155–11160, 2022.

[22] L. Y. Yin, Z. H. Xue, W. Ren, *et al*., "High-roll-off-rate ultrathin polarization-rotating frequency selective surface," *IEEE Antennas and Wireless Propagation Letters*, vol. 22, no. 7, pp. 1592–1596, 2023.

[23] X. Gao, X. Han, W. P. Cao, *et al*., "Ultrawideband and high-efficiency linear polarization converter based on double V-shaped metasurface," *IEEE Transactions on Antennas and Propagation*, vol. 63, no. 8, pp. 3522–3530, 2015.

[24] X. J. Huang, H. L. Yang, D. H. Zhang, *et al*., "Ultrathin dual-band metasurface polarization converter," *IEEE Transactions on Antennas and Propagation*, vol. 67, no. 7, pp. 4636–4641, 2019.

[25] W. R. Li, H. K. Guo, X. Y. Wang, *et al*., "A 2-bit reconfigurable metasurface with real-time control for deflection, diffusion, and polarization," *IEEE Transactions on Antennas and Propagation*, vol. 72, no. 2, pp. 1521–1531, 2024.

[26] X. Y. Fang, X. Z. Zheng, M. M. Li, *et al*., "Wireless secure communication based on code domain space-time modulated metasurface," *Electromagnetic Science*, vol. 2, no. 4, article no. 0080352, 2024.

[27] Y. J. Feng, Q. Hu, K. Qu, *et al*., "Reconfigurable intelligent surfaces: Design, implementation, and practical demonstration," *Electromagnetic Science*, vol. 1, no. 2, article no. 0020111, 2023.

[28] C. H. Liu, F. Yang, S. H. Xu, *et al*., "Reconfigurable metasurface: A systematic categorization and recent advances," *Electromagnetic Science*, vol. 1, no. 4, article no. 0040021, 2023.

[29] G. Perez-Palomino, P. Baine, R. Dickie, *et al*., "Design and experimental validation of liquid crystal-based reconfigurable reflectarray elements with improved bandwidth in F-band," *IEEE Transactions*

on Antennas and Propagation, vol. 61, no. 4, pp. 1704–1713, 2013.
[30] I. Jung, Z. Peng, and Y. Rahmat-Samii, "Recent advances in reconfigurable electromagnetic surfaces: Engineering design, full-wave analysis, and large-scale optimization," *Electromagnetic Science*, vol. 2, no. 3, article no. 0070201, 2024.
[31] S. Dash, C. Psomas, I. Krikidis, *et al*., "Active control of THz waves in wireless environments using graphene-based RIS," *IEEE Transactions on Antennas and Propagation*, vol. 70, no. 10, pp. 8785–8797, 2022.
[32] G. B. Wu, J. Y. Dai, Q. Cheng, *et al*., "Sideband-free space-time-coding metasurface antennas," *Nature Electronics*, vol. 5, no. 11, pp. 808–819, 2022.
[33] P. Y. Chen and A. Alù, "Mantle cloaking using thin patterned metasurfaces," *Physical Review B*, vol. 84, no. 20, article no. 205110, 2011.
[34] Y. J. Liu, N. Qi, Z. B. Pang, *et al*., "Metasurface-based modulation with enhanced interference resilience," *IEEE Communications Letters*, vol. 27, no. 5, pp. 1447–1451, 2023.
[35] L. L. Li, T. J. Cui, W. Ji, *et al*., "Electromagnetic reprogrammable coding-metasurface holograms," *Nature Communications*, vol. 8, no. 1, article no. 197, 2017.
[36] D. X. Xia, L. Guan, H. X. Liu, *et al*., "MetaBreath: Multitarget respiration detection based on space-time-coding digital metasurface," *IEEE Transactions on Microwave Theory and Techniques*, vol. 72, no. 2, pp. 1433–1443, 2024.
[37] E. A. Parker and A. N. A. El Sheikh, "Convoluted dipole array elements," *Electronics Letters*, vol. 27, no. 4, pp. 322–323, 1991.
[38] C. Jin, Q. H. Lv, B. C. Zhang, *et al*., "Ultra-wide-angle bandpass frequency selective surface," *IEEE Transactions on Antennas and Propagation*, vol. 69, no. 9, pp. 5673–5681, 2021.
[39] Q. H. Lv, C. Jin, B. C. Zhang, *et al*., "Ultrawide-angle ultralow-reflection phenomenon for transverse electric mode in anisotropic metasurface," *Advanced Optical Materials*, vol. 10, no. 12, article no. 2102400, 2022.
[40] J. J. Du, Z. F. Lin, S. T. Chui, *et al*., "Nearly total omnidirectional reflection by a single layer of nanorods," *Physical Review Letters*, vol. 110, no. 16, article no. 163902, 2013.
[41] W. Liu, "Generalized magnetic mirrors," *Physical Review Letters*, vol. 119, no. 12, article no. 123902, 2017.
[42] J. Luo, Y. T. Yang, Z. Q. Yao, *et al*., "Ultratransparent media and transformation optics with shifted spatial dispersions," *Physical Review Letters*, vol. 117, no. 22, article no. 223901, 2016.
[43] H. Luo, J. Luo, Z. H. Zhang, *et al*., "Dielectric metamaterials with effective self-duality and full-polarization omnidirectional brewster effect," *Light: Science & Applications*, vol. 13, no. 1, article no. 262, 2024.
[44] T. T. Song, H. C. Chu, J. Luo, *et al*., "Ultracompact photonic circuits without cladding layers," *Physical Review X*, vol. 12, no. 1, article no. 011053, 2022.
[45] H. Huang and Z. X. Shen, "Angle-selective surface based on uniaxial dielectric-magnetic slab," *IEEE Antennas and Wireless Propagation Letters*, vol. 19, no. 12, pp. 2457–2461, 2020.
[46] Z. T. Chen, C. Du, J. Liu, *et al*., "Design methodology of dual-polarized angle-selective surface based on three-layer frequency-selective surfaces," *IEEE Transactions on Antennas and Propagation*, vol. 71, no. 11, pp. 8704–8713, 2023.
[47] Y. J. Hong and Z. X. Shen, "Dual-polarized bilayer angle-selective structure," *IEEE Antennas and Wireless Propagation Letters*, vol. 23, no. 2, pp. 823–827, 2024.
[48] Y. Gao, B. H. Li, R. Wang, *et al*., "Polarization-independent broadband angular selectivity based on anisotropic diamagnetic metamaterial," *IEEE Transactions on Antennas and Propagation*, vol. 70, no. 8, pp. 7306–7310, 2022.
[49] X. Chen, Z. J. Wang, W. C. Chen, *et al*., "Magnetic metamirrors as spatial frequency filters," *IEEE Transactions on Antennas and Propagation*, vol. 68, no. 7, pp. 5505–5511, 2020.
[50] X. D. Chen, T. M. Grzegorczyk, B. I. Wu, *et al*., "Robust method to retrieve the constitutive effective parameters of metamaterials," *Physical Review E*, vol. 70, no. 1, article no. 016608, 2004.
[51] J. B. Pendry, A. J. Holden, D. J. Robbins, *et al*., "Magnetism from conductors and enhanced nonlinear phenomena," *IEEE Transactions on Microwave Theory and Techniques*, vol. 47, no. 11, pp. 2075–2084, 1999.
[52] Q. H. Lv, X. Qin, M. Z. Hu, *et al*., "Metatronics-inspired high-selectivity metasurface filter," *Nanophotonics*, vol. 13, no. 16, pp. 2995–3003, 2024.
[53] Y. C. He and G. V. Eleftheriades, "Magnetoelectric uniaxial metamaterials as wide-angle polarization-insensitive matching layers," *Physical Review B*, vol. 98, no. 20, article no. 205404, 2018.
[54] Q. H. Lv, R. P. Cui, P. H. Li, *et al*., "High-selectivity electromagnetic absorption with milli-wavelength-thick flexible metagraphene," *Materials Science and Engineering: R: Reports*, vol. 166, article no. 101067, 2025.

Qihao Lv received the B.S. degree in communication engineering from Nanjing University of Science and Technology, Nanjing, China, in 2016, and the Ph.D. degree from Beijing Institute of Technology, Beijing, China, in 2022. In July 2022, he became a Postdoctoral Fellow with the Department of Electronics Engineering, Tsinghua University, Beijing, China. He is currently a Research Fellow with the School of Electrical and Electronic Engineering, Nanyang Technological University, Singapore. His current research interests include metamaterials, frequency selective surfaces, as well as microwave and millimeter-wave antennas.

Dr. Lv has served on review boards for various technical journals, including *IEEE Transactions on Antenna and Propagation*, *IEEE Transactions on Microwave Theory and Techniques*, and *IEEE Antennas and Wireless Propagation Letters*.
(Email: qihao.lyu@ntu.edu.sg)

Yufei Zhao received the B.Eng. degree (Outstanding Graduates) in electronic information engineering from Harbin Institute of Technology, Harbin, China, in 2014, and the Ph.D. degree in aeronautical and astronautical science and technology from Tsinghua University, Beijing, China, in 2020. From 2020 to 2021, he worked as a Senior Engineer at Huawei Technologies Company Ltd., Beijing, China. He is now a Research Fellow at the School of Electrical and Electronic Engineering, Nanyang Technological University, Singapore. His current research interests include wireless communication engineering, radio-frequency (RF) & microwave system, reconfigurable intelligent surface (RIS), and electromagnetic wave transmission with orbital angular momentum (OAM).

Dr. Zhao has published more than 50 journal and conference papers. He has 2 filed patents and 5 granted patents. He serves as a reviewer for *IEEE Transactions on Antennas and Propagation*, *IEEE Transacations on Wireless Communications*, *IEEE Transactions on Vehicular Technology*, and *IEEE Internet of Things Journal*. He served as the session chair for the 2024 IEEE Vehicular Technology Conference (VTC2024-Spring) and the 2024 Asia Pacific Microwave Conference (APMC 2024). He was also the recipient of the Young Scientist Award in both 2022 and 2024, Singapore Workshop on Antenna.
(Email: yufei.zhao@ntu.edu.sg)

Yong Liang Guan obtained the Ph.D. degree from Imperial College London, London, UK, and the B.Eng. degree with first class honours from National University of Singapore, Singapore. He is now a Professor of communication engineering at the School of Electrical and Electronic Engineering, Nanyang Technological University (NTU), Singapore, where he leads the Continental-NTU Corporate Research Lab and led the successful deployment of the campus-wide NTU-NXP V2X Test Bed. His research interests broadly include coding and signal processing for communication systems and data storage systems.

Dr. Guan has published an invited monograph, 2 books, and more than 450 journal and conference papers. He has secured over $70 million of external research funding. He has 15 filed patents and 3 granted patents, one of which was licensed to NXP Semiconductors. He is an Editor for *IEEE Transactions on Vehicular Technology*. Currently he is also an Associate Vice President of NTU and a Distinguished Lecturer of the IEEE Vehicular Technology Society.

(Email: EYLGuan@ntu.edu.sg)

Cheng Jin received the B.Eng. degree in electronic engineering from University of Electronic Science and Technology of China (UESTC), Chengdu, China, in 2007, and the Ph.D. degree in communication engineering from Nanyang Technological University (NTU), Singapore, in 2012. From 2011 to 2013, he was with the Institute of Microelectronics, Agency for Science, Technology and Research, Singapore. He is currently a Professor with the School of Cyberspace Science and Technology, Beijing Institute of Technology, Beijing, China. He has authored and presented over 60 technical articles in journals/conferences. His current research interests include the design of microwave and millimeter-wave antennas, frequency-selective surfaces and circuits, and microwave radar techniques.

Dr. Jin was a TPC Member of the 2014 IEEE Symposium on Wireless Technology and Applications (ISWTA 2014). He was a recipient of the 2011 ICICS Recognition of High Quality Paper Award, Singapore, and the 2012 IEEE Singapore MTT/AP Chapter Best Student Paper Contest Award. He has served on review boards for various technical journals, including *IEEE Transactions on Antenna and Propagation*, *IEEE Antenna and Wireless Propagation Letters*, *IEEE Transactions on Microwave Theory and Techniques*, *IEEE Microwave and Wireless Components Letters*, and *IET Electronics Letters*. He was a Designated Reviewer of the ISWTA 2013.

(Email: jincheng@bit.edu.cn)

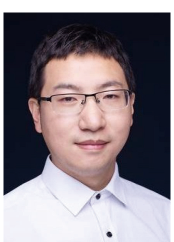

Yue Li received the B.S. degree in telecommunication engineering from Zhejiang University, Hangzhou, Zhejiang, China, in 2007, and the Ph.D. degree in electronic engineering from Tsinghua University, Beijing, China, in 2012. In June 2012, he was a Postdoctoral Fellow with the Department of Electronic Engineering, Tsinghua University, Beijing, China. In December 2013, he was a Research Scholar with the Department of Electrical and Systems Engineering, University of Pennsylvania, Philadelphia, PA, USA. He was also a Visiting Scholar with the Institute for Infocomm Research (2R), A*STAR, Singapore, in 2010, and Hawaii Center of Advanced Communication (HCAC), University of Hawaii at Manoa, Honolulu, Hl, USA, in 2012. Since January 2016, he has been with Tsinghua University, Beijing, China, where he is currently an Assistant Professor and an Associate Professor with the Department of Electronic Engineering. He has authored and co-authored over 260 journal articles and 50 international conference papers. He holds 26 granted Chinese patents. His current research interests include metamaterials, plasmonics, electromagnetics, nanocircuits, mobile and handset antennas, multi-input multi-output (MlMO) and diversity antennas, and millimeter-wave antennas and arrays.

Dr. Li was a recipient of the Issac Koga Gold Medal from the General Assembly of International Union of Radio Science (URSI). He served as an Associate Editor for *IEEE Transactions on Antennas and Propagation* and *IEEE Antennas and Wireless Propagation Letters* fom 2017 to 2024. He is also serving as an Associate Editor for *Microwave and Optical Technology Letters* and *Computer Applications in Engineering Education*.

(Email: lyee@tsinghua.edu.cn)

Chau Yuen received the B.Eng. and Ph.D. degrees from Nanyang Technological University, Singapore, in 2000 and 2004, respectively. He was a Post-Doctoral Fellow with Lucent Technologies Bell Labs, Murray Hill, NJ, USA, in 2005. From 2006 to 2010, he was with the Institute for Infocomm Research, Singapore. From 2010 to 2023, he was with the Engineering Product Development Pillar, Singapore University of Technology and Design, Singapore. Since 2023, he has been with the School of Electrical and Electronic Engineering, Nanyang Technological University, Singapore, where he is currently the Provost's Chair in wireless communications, Assistant Dean of the Graduate College, and Cluster Director for Sustainable Built Environment at ERI@N. Dr. Yuen received IEEE Communications Society Leonard G. Abraham Prize (2024), IEEE Communications Society Best Tutorial Paper Award (2024), IEEE Communications Society Fred W. Ellersick Prize (2023), IEEE Marconi Prize Paper Award in Wireless Communications (2021), IEEE APB Outstanding Paper Award (2023), and EURASIP Best Paper Award for *Journal on Wireless Communications and Networking* (2021). He is listed as Top 2% Scientists by Stanford University, and also a Highly Cited Researcher by Clarivate Web of Science from 2022.

(Email: chau.yuen@ntu.edu.sg)